Fermi Surface and Mass Renormalization in the Iron-Based Superconductor YFe_2Ge_2

Jordan Baglo,[1,†] Jiasheng Chen,[1] Keiron Murphy,[1] Roos Leenen,[2] Alix McCollam,[2] Michael L. Sutherland,[1] and F. Malte Grosche[1,*]

[1]*Cavendish Laboratory, University of Cambridge, Cambridge CB3 0HE, United Kingdom*
[2]*High Field Magnet Laboratory (HFML-EMFL), Radboud University, 6525 ED Nijmegen, Netherlands*

(Received 23 April 2021; revised 19 March 2022; accepted 27 May 2022; published 20 July 2022)

Interaction-enhanced carrier masses are central to the phenomenology of iron-based superconductors. Quantum oscillation measurements in the new unconventional superconductor YFe_2Ge_2 resolve all four Fermi surface pockets expected from band structure calculations, which predict an electron pocket in the Brillouin zone corner and three hole pockets enveloping the centers of the top and bottom of the Brillouin zone. Carrier masses reach up to 20 times the bare electron mass and are among the highest ever observed in any iron-based material, accounting for the enhanced heat capacity Sommerfeld coefficient $\simeq 100\ \mathrm{mJ/mol\,K^2}$. Mass renormalization is uniform across reciprocal space, suggesting predominantly local correlations, as in the Hund's metal scenario.

DOI: 10.1103/PhysRevLett.129.046402

Superconductivity in iron pnictides and chalcogenides emerges from a rich interplay of magnetic, structural, and nematic instabilities as well as the associated quantum critical phenomena [1–4]. This diverse phenomenology includes strong quasiparticle mass renormalization, which in the extreme case of the alkali metal iron arsenides $(K/Rb/Cs)Fe_2As_2$ produces heat capacity Sommerfeld coefficients $\sim$100–200 $\mathrm{mJ/mol\,K^2}$. Although the Sommerfeld coefficient approaches a level usually associated with rare-earth-based heavy fermion materials, it occurs without their partially filled f states. Resolving this conundrum would present key insights into the strong correlation physics of iron-based superconductivity. One approach could consider primarily the effects of long-ranged magnetic fluctuations that emerge near the threshold of magnetic order, at a so-called quantum critical point, and which may also underlie the pairing mechanism. An alternative explanation for the strong mass renormalization might instead focus on a more local mechanism like the Kondo effect [5]. In Fe-based materials, this may be amplified by Hund's rule coupling, which locks the iron d electrons into a high spin state and thereby boosts electronic correlations [6–11]. Because magnetic fluctuations peak at specific critical wave vectors, they would be expected to enhance quasiparticle masses on certain "hot" regions on the Fermi surface, which are connected by the critical wave vectors, producing nonuniform mass renormalization. The strong correlations induced by on site interactions as in the Kondo lattice-Hund's metal picture, by contrast, are local and therefore less selective in reciprocal space. Quantum oscillation measurements present an opportunity to distinguish the two scenarios experimentally.

We examine the origin of mass renormalization in iron-based intermetallics in the iron germanide superconductor YFe_2Ge_2 [12–14]. It shares key aspects with the alkali metal iron arsenides $(K/Rb/Cs)Fe_2As_2$, such as (i) bad metal behavior at high temperature T, with resistivities ρ of several hundred $\mu\Omega$cm, (ii) low transition temperatures T_c of order a few kelvin, (iii) strongly enhanced heat capacity Sommerfeld coefficient $\gamma_n \simeq 100\ \mathrm{mJ/mol\,K^2}$, (iv) reduced heat capacity jump at T_c of order $0.4T_c\gamma_n$, and (v) residual extrapolated C/T at low T of order $0.4\gamma_n$ [15,16]. On the other hand, it lacks the pnictogen or chalcogen constituents of other Fe-based superconductors, and because the Ge layers in YFe_2Ge_2 are covalently bonded along $\hat{c}$, it forms a more compressed, collapsed-tetragonal structure. Density functional theory (DFT) calculations [17,18] suggest that this leads to a much more strongly warped Fermi surface (FS) geometry than the cylindrical FS sheets found in other iron-based superconductors (Fig. 1). Key input for any comprehensive theoretical description of iron-based superconductors derives from the experimental determination of the electronic structure by photoemission spectroscopy or quantum oscillation measurements (e.g., [19–21]). In YFe_2Ge_2, an early ARPES study [22] investigated the electronic structure, and core-level spectroscopy indicated a large fluctuating Fe moment $\simeq 1\ \mu_B$ [23], which is consistent with neutron scattering and NMR studies [24,25]. The precise determination of Fermi surface and carrier mass by quantum oscillation techniques, however, has in YFe_2Ge_2 so far been held back by the lack of single crystals with the required level of purity [26]. Here, we present a detailed study of Fermi surface structure and carrier mass by observing de Haas–van Alphen oscillations in a new generation of high-quality crystals of YFe_2Ge_2. We find

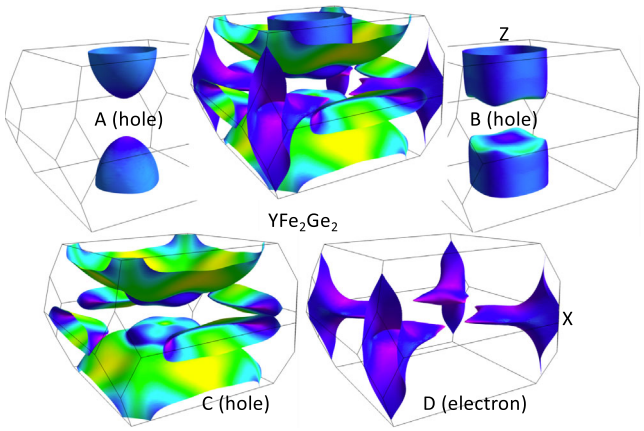

FIG. 1. *Ab initio* Fermi surface structure of YFe_2Ge_2. The Fermi surface (top center) consists of three concentric hole pockets (A-C), which envelop the Z point on the Brillouin zone (BZ) boundary, and a single electron pocket (D) centered on the X point at the corner of the BZ. Lighter colors indicate higher Fermi velocity. The *ab initio* orbital character does not separate out straightforwardly for the different Fermi surface sheets, as d_{xz} and d_{yz} contribute to band states on A and D, supplemented by d_{xy} on B and by d_{xy} and d_{z^2} on C [17,18].

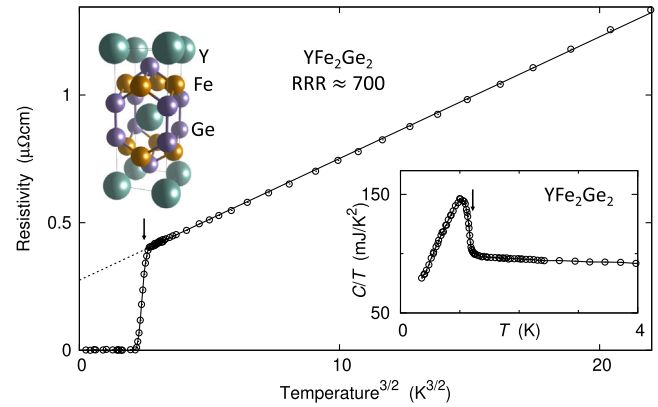

FIG. 2. Low temperature properties of YFe_2Ge_2. The in-plane electrical resistivity $\rho(T)$ displays a superconducting transition (arrow) below an anomalous normal-state $T^{3/2}$ form. A sharp superconducting anomaly (arrow) is also observed in the heat capacity Sommerfeld ratio C/T (inset), which in the normal state reaches $\simeq 100\ \mathrm{mJ/mol\,K^2}$.

that the Fermi surface consists of three hole pockets and one electron pocket, with shapes broadly in line with numerical calculations [17,18]. Carrier masses are enhanced roughly fivefold over DFT values. The mass renormalization varies only weakly between Fermi surface pockets and within each Fermi surface pocket, suggesting that on site interactions provide the primary mechanism for the profound mass enhancement and boost to the electronic heat capacity recorded in YFe_2Ge_2.

High-purity crystals of YFe_2Ge_2 were grown by a liquid transport technique [27,28] and characterized by electrical transport, magnetic, and thermodynamic measurements. They display sharp superconducting transition anomalies (Fig. 2), and their residual resistivities are $\simeq 0.3\ \mu\Omega\,\mathrm{cm}$, corresponding to residual resistance ratios $\mathrm{RRR} = \rho(300\,\mathrm{K})/\rho_0 \simeq 700$. Angle-dependent de Haas–van Alphen measurements at fields of up to 18 T were performed using a mutual inductance technique with modulation field amplitude $\simeq 0.2$ mT at a frequency of ~ 29 Hz on two samples ($S1, S2$) in a superconducting cryomagnet-dilution refrigerator system at the Cavendish Laboratory, and using piezoresistive torque magnetometry on a third sample ($S3$) at fields of up to 38 T in a resistive electromagnet-dilution refrigerator system at HFML Nijmegen. Sample $S1$ ($S2$) was mounted with the crystallographic $\hat{c}$ ($\hat{a}$) direction aligned with the axis of the respective pickup coil, and $S3$ was mounted with $\hat{c}$ perpendicular to the surface of the cantilever. Quantum oscillation data were extracted by subtracting a low-order polynomial background from the raw data, and oscillations periodic in $1/B$ were identified from peaks in the power spectrum. The peak frequencies F relate to extremal cross-sectional areas A_k of the Fermi surface via the Onsager relation $A_k = (2\pi e/\hbar)F$. The dependence of the signal amplitude $\tilde{y}$ on temperature T at a fixed magnetic field B provides the effective carrier mass m^* via the Lifshitz-Kosevich expression $\tilde{y} = \alpha T\{\sinh[14.639\,\mathrm{TK^{-1}}(T/B)(m^*/m_e)]\}^{-1}$, where α is a temperature-independent factor and m_e is the bare electron mass. The field dependence of the signal envelope provides an estimate of the electronic mean free path [29,30]. The electronic structure was calculated using the generalized gradient approximation [32] in WIEN2k [33] with 100 000 k points in the BZ (6768 k points in the irreducible BZ) and $Rk_{\max} = 7$, using the experimentally determined crystal structure at 100 K with $a = 3.95917(3)$ Å, $c = 10.39754(13)$ Å, and the fractional vertical Ge position $z = 0.378331(7)$ [27]. Extremal orbits, band masses, and pocket-resolved contributions to the density of states (DOS) were extracted using SKEAF [34], and Fermi surfaces were plotted in FermiSurfer [35].

The calculated Fermi surface (Fig. 1) consists of three roughly ellipsoidal hole pockets (A–C) nested around Z at the top and bottom of the Brillouin zone and a roughly cylindrical electron pocket (D) around X at the zone corner, with a duckbill-shaped outgrowth toward the center of the BZ at Γ. Moreover, our DFT calculations produce an unrenormalized Sommerfeld coefficient $\gamma_0 \simeq 16.7\ \mathrm{mJ/mol\,K^2}$, a factor of six less than the experimentally observed value but significantly larger than values previously obtained in calculations based on numerically relaxed z parameters [17,18].

The quantum oscillation (QO) signal observed in $S1$ (Fig. 3) displays three fundamental frequencies, α, β, and γ. The same set of frequencies is present in sample $S2$, as shown in the Supplemental Material [30]. The results of a rotation study from $H \| \hat{c}$ ($\theta = 0°$) to $H \| \hat{a}$ ($\theta = 90°$) are summarized in Figs. 3(b) and 4(a). The three fundamental

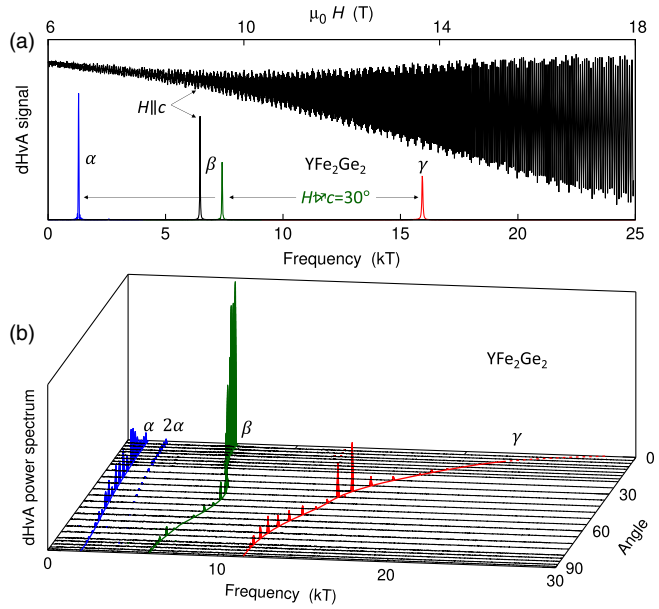

FIG. 3. De Haas–van Alphen signal. (a) Strong oscillations are observed in sample $S1$ for $B\|c$ down to fields < 6 T (black trace and associated black peak in power spectrum). At a tilt angle $\theta = 30°$, three fundamental frequencies α, β, and γ as well as some harmonics can be resolved. (b) The evolution of these frequencies with tilt angle suggests that they can be assigned to orbits on sheets A, B, and C, respectively (Fig. 1, see text).

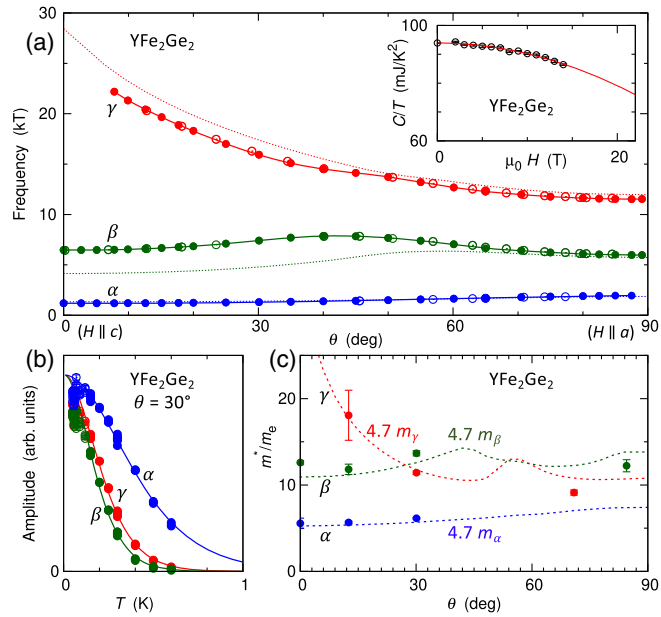

FIG. 4. Quantum oscillation results for the three hole pockets. (a) Frequencies (filled symbols, $S1$; open symbols, $S2$) as function of angle, rotating from $H\|\hat{c}$ ($\theta = 0°$) to $H\|\hat{a}$ ($\theta = 90°$). Dotted lines show DFT results. A band shift of -10 mRyd was used for α (Table I). Inset: field dependence of the Sommerfeld ratio at $T = 1.5$ K. (b) Temperature dependence of the oscillation amplitudes extracted in $S1$ for 16 T $< B <$ 18 T at $\theta = 30°$. Solid lines show Lifshitz-Kosevich fits to the data at $T > 0.12$ K. (c) Angle dependence of the extracted effective masses for the α, β, and γ orbits compared to DFT band masses $m_{\alpha,\beta,\gamma}$, uniformly renormalized by $\times 4.7$ (dashed lines).

frequencies α, β, and γ were tracked over most of the angular range. By comparing to the DFT results, they can be assigned to extremal orbits on the three hole pockets. The highest frequency, γ, is unambiguously associated with the largest hole pocket, C. The next highest frequency, β, matches predictions for the second hole sheet (B), with good quantitative agreement near $H\|\hat{a}$. The third frequency, α, depends weakly on tilt angle, as expected for the smallest, nearly ellipsoidal hole pocket (A), but at roughly half the predicted frequency. The effective masses extracted from Lifshitz-Kosevich fits [Fig. 4(b)] are high, with m^* exceeding 10 m_e on the γ and β sheets. These values markedly exceed the highest masses measured in the $BaFe_2(As/P)_2$ series [36] and are as high as those observed in $(K/Rb/Cs)Fe_2As_2$ [21,37,38]. Whereas effective masses for α and β show little angle dependence, that of γ rises sharply near $H\|\hat{c}$ [Fig. 4(c)]. A uniform renormalization of DFT band masses by $\sim$5 produces good agreement with experimental values on all three hole pockets.

The electron pocket D could not be resolved at fields of up to 18 T. Its *ab initio* volume corresponds to 0.142 electrons/formula unit (f.u.), and its expected dominant QO frequency is $\sim$0.9 kT. This estimate can be refined by using the QO data on the three observed hole pockets in combination with charge neutrality, which imposes an overall hole count of 1/formula unit. Assuming that the *ab initio* geometry and associated hole count n_0 of each hole pocket can be scaled to make them consistent with the measured QO frequencies, we estimate the actual hole count for each pocket as $n = n_0 q_a^2 q_c/(q_{0,a}^2 q_{0,c}) \propto \sqrt{F_a^2 F_c}/\sqrt{F_{0,a}^2 F_{0,c}}$. Here, $F_a \propto q_a q_c$, the QO frequency for field along $\hat{a}$, is given by the extent q_a, q_c of the pocket along $\hat{a}$ and $\hat{c}$, and $F_c \propto q_a^2$, the QO frequency for field along $\hat{c}$, is determined by the extent of the pocket $\perp\hat{c}$, or along $\hat{a}$. $F_{0,a}$ and $F_{0,c}$ are the *ab initio* frequencies for the same pocket, and $q_{0,a}$, $q_{0,c}$ the corresponding dimensions. In the case of pocket C, the γ frequency was extrapolated to $\theta = 0°$, and the resulting hole count checked for consistency against a second calculation in which F_c and $F_{0,c}$ values were taken at $\theta = 7.5°$, the lowest angle at which the γ oscillation could be observed. The upper half of Table I summarizes the results of these calculations, which suggest that the total hole count per f.u. arising from A, B and C is about 1.07. This implies that the volume of the electron pocket is smaller than expected from *ab initio* calculations. It corresponds to about $0.07e^-$ per f.u., which leads to a dominant QO frequency of order 500 T. A clear signature of oscillations in this frequency range was seen in torque magnetometry to fields of up to 38 T in sample $S3$ (Fig. 5).

TABLE I. Particle number and DOS budgets in YFe_2Ge_2. DFT Fermi surface pocket volumes for the hole pockets A–C (top line) have been corrected by using the measured cross-sectional areas (second line, see text). The requirement to reach 1 hole/f.u. fixes the volume of the electron pocket D. The third data line lists the band shifts that bring each pocket in line with the QO-corrected hole count. The *ab initio* DOS (fourth data line, converted to C/T) calculated for the experimentally determined fractional vertical Ge coordinate $z = 0.37833$ is dominated by the contribution from the electron pocket D. The analogous calculation for the shifted bands produces a lower contribution from the hole pockets, shifting the balance even more toward the electron pocket. Applying the mass renormalization ≃4.7 estimated from QO measurements (Fig. 4) to the calculated DOS produces an overall C/T in rough agreement with experiment.

FS pocket	A	B	C	$\sum_{A-C}$	D
Hole count	f.u.$^{-1}$	...	...	...	...
Ab initio	0.098	0.208	0.836	1.142	−0.142
QO-corrected	0.029	0.271	0.769	1.069	−0.069
ΔE (mRyd)	−10	3.5	−2.4	...	1.6

FS pocket	A	B	C	D	$4.7\sum_{A-D}$
C/T	mJ/mol K^2	...	...	...	...
Ab initio	1.68	2.95	5.30	6.81	78.5
QO-corrected	0.79	3.34	4.43	7.58	75.9

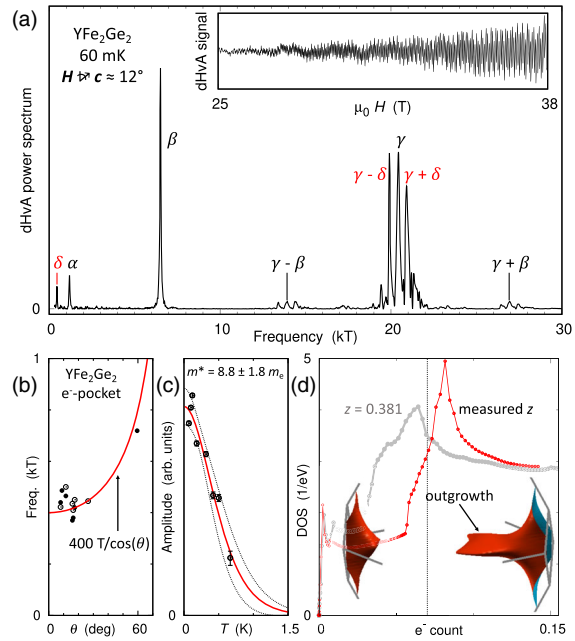

FIG. 5. Electron pocket in YFe_2Ge_2. (a) Quantum oscillations in the magnetic torque occur at the frequencies expected for the three hole pockets α, β, and γ, but the nonlinear response of the cantilever torque sensor produces side lobes to the γ frequency which can be indexed as $\gamma \pm \delta$, where $\delta \simeq 450$ T is attributed to the electron pocket located in the BZ corner. A peak at the same frequency δ is observed at some field angles. (b) Tracking δ via the side-lobe frequency (open symbols) and stand-alone peak frequency (closed symbols) reveals an angle dependence that is consistent with a cylindrical pocket, for which the cross-sectional area is $\propto 1/\cos(\theta)$. (c) A Lifshitz-Kosevich fit to the amplitude extracted at an angle of ≃60° reveals a strongly enhanced carrier mass $m^* = 8.8 \pm 1.8\ m_e$. (d) The electron pocket DOS peaks sharply at a critical band filling that depends on z, as a duckbill outgrowth appears.

Our initial observation exploited the phenomenon of torque interaction [29–31], which mixes quantum oscillation frequencies via the nonlinear cantilever response at high magnetic fields. The γ peak develops several side lobes, some of which can be indexed as $\gamma \pm n\delta$ with $\delta \sim 450$ T, depending on the field angle. At some angles, a distinct low-frequency peak at the corresponding frequency δ can also be resolved directly (Fig. 5). Further work will be required to narrow down the current mass estimate $m^* \simeq 8.8 \pm 1.8\ m_e$ obtained at a 60° tilt angle from the temperature dependence of the directly observed peak intensity [Fig. 5(c)], and to track the mass as a function of angle. Because the angle dependence [Fig. 5(b)] is consistent with a small cylindrical pocket, we interpret δ as a signature of the elusive electron pocket D. The DOS contribution of the electron pocket is highly sensitive to details such as band filling and the structural z parameter. This sensitivity is caused by a flat region in the dispersion along the BZ diagonal, which produces a duckbill outgrowth toward the center of the BZ. As this feature is quasi-1D (little dispersion within the symmetry plane of the BZ), its emergence produces a van Hove-like singularity in the DOS [Fig. 5(d)]. YFe_2Ge_2 appears to be situated close to the cusp of this anomaly, similar to the situation of the γ sheet in Sr_2RuO_4 (e.g., Ref. [39]).

The lower part of Table I tracks the contributions of the different Fermi surface pockets to the overall DOS. When the bands are shifted to bring the DFT pocket volumes into line with QO data, the resulting "QO-corrected" DOS is dominated by the electron pocket, which contributes nearly half of the total DOS. Applying a uniform mass renormalization of 4.7 across all pockets A–D, as suggested by the high-resolution measurements for pockets A–C (Fig. 4) would account for a normal-state Sommerfeld ratio $C/T \simeq 76$ mJ/mol K^2 at ≃18 T, where QO masses are extracted. The shortfall of about 20% compared to C/T at zero field could be attributed in part to the experimentally observed reduction in C/T in high magnetic field [inset Fig. 4(a)], as magnetic fluctuations are increasingly suppressed and in part to uncertainty in ascertaining the precise DOS contribution associated with the electron pocket, as mentioned above.

Our findings establish the electronic structure of YFe_2Ge_2 as consistent with expectations from *ab initio* calculations, but with strong, uniform mass renormalization on all Fermi surface sheets. This suggests an underpinning, robust mass enhancement caused by on site correlations, as in the Kondo lattice-Hund's metal scenario [5–11]. Further

to this local mechanism, *long-ranged* magnetic correlations observed in neutron scattering [24] and consistent with the magnetic order observed in the antiferromagnetic isoelectronic sister compound $LuFe_2Ge_2$ [40] may underlie the superconducting pairing interaction as well as the non-Fermi liquid $T^{1.5}$ resistivity power law. The combination of a robust mass renormalization and a fine-tuned pairing interaction is strongly reminiscent of rare-earth-based Kondo lattice heavy fermion superconductors [41] and may apply more generally in strongly correlated transition metal compounds.

All data needed to evaluate the conclusions in the paper are present in the paper, the Supplementary Materials, and the Data Repository at the University of Cambridge and can be downloaded from [42].

We thank, in particular, G. Lonzarich for helpful discussions. The work was supported by the EPSRC of the UK (Grants No. EP/K012894/1, No. EP/P023290/1 and No. EP/N01085X/1), by Trinity College, and by the HFML-RU member of the European Magnetic Field Laboratory (EMFL).

*fmg12@cam.ac.uk

†Present address: Institut Quantique and Département de Physique, Université de Sherbrooke, Sherbrooke (Québec), J1K 2R1 Canada.

[1] H. Hosono and K. Kuroki, Physica (Amsterdam) **514C**, 399 (2015).

[2] Q. Si, R. Yu, and E. Abrahams, Nat. Rev. Mater. **1**, 16017 (2016).

[3] T. Shibauchi, A. Carrington, and Y. Matsuda, Annu. Rev. Condens. Matter Phys. **5**, 113 (2014).

[4] M. D. Watson, T. K. Kim, A. A. Haghighirad, N. R. Davies, A. McCollam, A. Narayanan, S. F. Blake, Y. L. Chen, S. Ghannadzadeh, A. J. Schofield, M. Hoesch, C. Meingast, T. Wolf, and A. I. Coldea, Phys. Rev. B **91**, 155106 (2015).

[5] Y. P. Wu, D. Zhao, A. F. Wang, N. Z. Wang, Z. J. Xiang, X. G. Luo, T. Wu, and X. H. Chen, Phys. Rev. Lett. **116**, 147001 (2016).

[6] K. Haule and G. Kotliar, New J. Phys. **11**, 025021 (2009).

[7] Z. P. Yin, K. Haule, and G. Kotliar, Nat. Mater. **10**, 932 (2011).

[8] A. Georges, L. de'Medici, and J. Mravlje, Annu. Rev. Condens. Matter Phys. **4**, 137 (2013).

[9] L. de'Medici, G. Giovannetti, and M. Capone, Phys. Rev. Lett. **112**, 177001 (2014).

[10] S. Backes, H. O. Jeschke, and R. Valentí, Phys. Rev. B **92**, 195128 (2015).

[11] D. Zhao, H. L. Wo, J. Li, D. W. Song, L. X. Zheng, S. J. Li, L. P. Nie, X. G. Luo, J. Zhao, T. Wu, and X. H. Chen, Phys. Rev. B **101**, 064511 (2020).

[12] Y. Zou, Z. Feng, P. W. Logg, J. Chen, G. Lampronti, and F. M. Grosche, Phys. Status Solidi RRL **8**, 928 (2014).

[13] J. Chen, K. Semeniuk, Z. Feng, P. Reiss, P. Brown, Y. Zou, P. W. Logg, G. I. Lampronti, and F. M. Grosche, Phys. Rev. Lett. **116**, 127001 (2016).

[14] J. Chen, M. B. Gamża, K. Semeniuk, and F. M. Grosche, Phys. Rev. B **99**, 020501(R) (2019).

[15] M. Avila, S. Bud'ko, and P. Canfield, J. Magn. Magn. Mater. **270**, 51 (2004).

[16] F. Hardy, A. E. Böhmer, D. Aoki, P. Burger, T. Wolf, P. Schweiss, R. Heid, P. Adelmann, Y. X. Yao, G. Kotliar, J. Schmalian, and C. Meingast, Phys. Rev. Lett. **111**, 027002 (2013).

[17] A. Subedi, Phys. Rev. B **89**, 024504 (2014).

[18] D. J. Singh, Phys. Rev. B **89**, 024505 (2014).

[19] A. I. Coldea, J. D. Fletcher, A. Carrington, J. G. Analytis, A. F. Bangura, J.-H. Chu, A. S. Erickson, I. R. Fisher, N. E. Hussey, and R. D. McDonald, Phys. Rev. Lett. **101**, 216402 (2008).

[20] T. Sato, K. Nakayama, Y. Sekiba, P. Richard, Y.-M. Xu, S. Souma, T. Takahashi, G. F. Chen, J. L. Luo, N. L. Wang, and H. Ding, Phys. Rev. Lett. **103**, 047002 (2009).

[21] T. Terashima, N. Kurita, M. Kimata, M. Tomita, S. Tsuchiya, M. Imai, A. Sato, K. Kihou, C.-H. Lee, H. Kito, H. Eisaki, A. Iyo, T. Saito, H. Fukazawa, Y. Kohori, H. Harima, and S. Uji, Phys. Rev. B **87**, 224512 (2013).

[22] D. F. Xu, D. W. Shen, D. Zhu, J. Jiang, B. P. Xie, Q. S. Wang, B. Y. Pan, P. Dudin, T. K. Kim, M. Hoesch, J. Zhao, X. G. Wan, and D. L. Feng, Phys. Rev. B **93**, 024506 (2016).

[23] N. Sirica, F. Bondino, S. Nappini, I. Píš, L. Poudel, A. D. Christianson, D. Mandrus, D. J. Singh, and N. Mannella, Phys. Rev. B **91**, 121102(R) (2015).

[24] H. Wo, Q. Wang, Y. Shen, X. Zhang, Y. Hao, Y. Feng, S. Shen, Z. He, B. Pan, W. Wang, K. Nakajima, S. Ohira-Kawamura, P. Steffens, M. Boehm, K. Schmalzl, T. R. Forrest, M. Matsuda, Y. Zhao, J. W. Lynn, Z. Yin, and J. Zhao, Phys. Rev. Lett. **122**, 217003 (2019).

[25] J. Srpčič, P. Jeglič, I. Felner, B. Lv, C. W. Chu, and D. Arčon, Phys. Rev. B **96**, 174430 (2017).

[26] H. Kim, S. Ran, E. Mun, H. Hodovanets, M. Tanatar, R. Prozorov, S. Bud'ko, and P. Canfield, Philos. Mag. **95**, 804 (2015).

[27] J. Chen, M. B. Gamża, J. Banda, K. Murphy, J. Tarrant, M. Brando, and F. M. Grosche, Phys. Rev. Lett. **125**, 237002 (2020).

[28] J.-Q. Yan, B. C. Sales, M. A. Susner, and M. A. McGuire, Phys. Rev. Mater. **1**, 023402 (2017).

[29] D. Shoenberg, *Magnetic Oscillations in Metals*, 1st ed. (Cambridge University Press, Cambridge, England, 1984).

[30] See Supplemental Material at http://link.aps.org/supplemental/10.1103/PhysRevLett.129.046402, which includes Refs. [29,31], for further details of QO results in sample S2, the Dingle analysis of the mean free path for both samples S1 and S2, the field dependence of the effective mass, and the torque interaction phenomenon (2022).

[31] J. Vanderkooy and W. R. Datars, Can. J. Phys. **46**, 1215 (1968).

[32] J. P. Perdew, K. Burke, and M. Ernzerhof, Phys. Rev. Lett. **77**, 3865 (1996).

[33] P. Blaha, K. Schwarz, F. Tran, R. Laskowski, G. K. H. Madsen, and L. D. Marks, J. Chem. Phys. **152**, 074101 (2020).

[34] P. Rourke and S. Julian, Comput. Phys. Commun. **183**, 324 (2012).

[35] M. Kawamura, Comput. Phys. Commun. **239**, 197 (2019).
[36] H. Shishido, A. F. Bangura, A. I. Coldea, S. Tonegawa, K. Hashimoto, S. Kasahara, P. M. C. Rourke, H. Ikeda, T. Terashima, R. Settai, Y. Ōnuki, D. Vignolles, C. Proust, B. Vignolle, A. McCollam, Y. Matsuda, T. Shibauchi, and A. Carrington, Phys. Rev. Lett. **104**, 057008 (2010).
[37] D. A. Zocco, K. Grube, F. Eilers, T. Wolf, and H. v. Löhneysen, J. Phys. Soc. Jpn. Conf. Proc. **3**, 015007 (2014).
[38] F. Eilers, K. Grube, D. A. Zocco, T. Wolf, M. Merz, P. Schweiss, R. Heid, R. Eder, R. Yu, J.-X. Zhu, Q. Si, T. Shibauchi, and H. v. Löhneysen, Phys. Rev. Lett. **116**, 237003 (2016).
[39] M. E. Barber, A. S. Gibbs, Y. Maeno, A. P. Mackenzie, and C. W. Hicks, Phys. Rev. Lett. **120**, 076602 (2018).
[40] T. Fujiwara, N. Aso, H. Yamamoto, M. Hedo, Y. Saiga, M. Nishi, Y. Uwatoko, and K. Hirota, J. Phys. Soc. Jpn. **76**, 60 (2007).
[41] N. D. Mathur, F. M. Grosche, S. R. Julian, I. R. Walker, D. M. Freye, R. K. W. Haselwimmer, and G. G. Lonzarich, Nature (London) **394**, 39 (1998).
[41] N. D. Mathur, F. M. Grosche, S. R. Julian, I. R. Walker, D. M. Freye, R. K. W. Haselwimmer, and G. G. Lonzarich, Nature (London) **394**, 39 (1998).
[42] 10.17863/CAM.85749.